

Adjoint-based Aeroacoustic Design-Optimization of Flexible Rotors in Forward Flight

Enrico Fabiano

PhD Candidate

University of Wyoming
Laramie, WY, U.S.

Dimitri Mavriplis

Professor

University of Wyoming
Laramie, WY, U.S.

ABSTRACT

This paper presents the development and application of a time-dependent adjoint-based method for aeroacoustic design optimization of flexible helicopter rotors in forward flight. The rotor noise signature at a farfield observer is computed with the hybrid aeroacoustic approach in which a near-body coupled computational fluid dynamics/computational structural dynamics solver provides flow and geometry data to an FW-H acoustic module that propagates the acoustic waves to a farfield observer. Forward and adjoint sensitivity formulations are derived that correspond to analogues of the multidisciplinary flexible aeroacoustic analysis problem. The newly implemented aeroacoustic capability is first verified to effectively perform forward flight noise prediction by comparison with the PSU-WOPWOP acoustic tool. Upon successful validation, a gradient based optimization method is used to minimize the required torque of the flexible HART-II rotor in trimmed forward flight while reducing the acoustic signature at a farfield observer by changing the shape of the blades. The adjoint formulation developed in this work is used to efficiently compute the sensitivity required by the optimization algorithm.

INTRODUCTION

As the importance of reducing detection distance and helicopter noise signature increases, rotor aeroacoustics take on a leading role in the helicopter design process. In the past, both passive and active noise reduction techniques have been investigated. Common passive noise minimization techniques consist of a judicious selection of rotor blade configurations, airfoils, planform and tip shapes (Ref. 1). Active control techniques such as Higher Harmonic Control (HHC), Individual Blade Control (IBC) and active flap configurations have also been investigated (Refs. 1–3). While traditional design approaches have treated the performance and aeroacoustic problem independently in a segregated manner, in this paper we investigate the use of numerical shape optimization techniques applied to the multidisciplinary design problem of required torque minimization of a rotor in forward flight with improved acoustic characteristics. However, because of the typical high flexibility of the rotor blades, aeroelastic coupling effects play a central role in both performance (Ref. 4) and noise signature prediction (Ref. 5). For this reason, our multidisciplinary design optimization approach combines the three disciplines of aerodynamics, aeroelasticity and aeroacoustics to determine the optimal flexible rotor shape that minimizes the rotor’s required torque in trimmed forward flight while reducing the noise signature at a far field observer. Few similar attempts have been made in the past, focusing mainly on two-dimensional applications (Refs. 6, 7), sonic-boom problems

for fixed wing aircraft (Ref. 8), or more recently, on propeller blade optimization (Ref. 9). In this work a gradient based sequential quadratic programming algorithm is used to find the optimal shape that will reduce the farfield noise signature of the flexible HART-II rotor in trimmed forward flight without incurring any torque penalty. The flexible aeroacoustic sensitivities used to drive the optimization are evaluated with the adjoint method, which offers the advantage of computing the sensitivity of an objective function with respect to any number of design variables at a cost roughly equivalent to a single analysis solution. While adjoint techniques for steady-state shape optimization problems are now well established in the aircraft industry (Refs. 10–13), their application to unsteady problems has received less attention (Refs. 14–16) because of the inherent computational cost and the complexity of the associated flow physics. Time dependent aerodynamic optimization for rotorcraft problems has been addressed by Nielsen et al. (Refs. 17, 18) and by Mani et al. (Ref. 19), while the inclusion of aeroelastic effects have been pursued by Mishra et al. (Refs. 20–22). In previous work (Ref. 7) we demonstrated the feasibility of unsteady aeroacoustic optimization by developing the coupled adjoint aeroacoustic sensitivity used to drive the gradient-based shape optimization of a two-dimensional airfoil in blade vortex interaction. We then extended our formulation to the noise minimization of a rigid helicopter rotor in trimmed forward flight (Ref. 23). Here we extend our aeroacoustic adjoint-based optimization capability by including blade aeroelastic effects to perform the noise minimization of flexible three-dimensional rotors in trimmed forward flight through the application of optimal shape modifications.

Presented at the AHS 72nd Annual Forum, West Palm Beach, Florida, May 17–19, 2016. Copyright © 2016 by the American Helicopter Society International, Inc. All rights reserved.

ANALYSIS FORMULATION

Flow Solver Formulation

The base flow solver used in this work is the NSU3D unstructured mesh Reynolds-averaged Navier-Stokes solver. NSU3D has been widely validated for steady-state and time-dependent flows and contains a discrete tangent and adjoint sensitivity capability which has been demonstrated previously for optimization of steady-state and time-dependent flow problems. As such, only a concise description of these formulations will be given in this paper, with additional details available in previous references (Refs. 19,24,25). The flow solver is based on the conservative form of the Navier-Stokes equations which may be written as:

$$\frac{\partial \mathbf{U}(\mathbf{x}, t)}{\partial t} + \nabla \cdot \mathbf{F}(\mathbf{U}) = 0 \quad (1)$$

For moving mesh problems these are written in arbitrary Lagrangian-Eulerian (ALE) form as:

$$\frac{\partial V \mathbf{U}}{\partial t} + \int_{aB(t)} [\mathbf{F}(\mathbf{U}) - \dot{\mathbf{x}} \mathbf{U}] \cdot \mathbf{n} dB = 0 \quad (2)$$

Here V refers to the area of the control volume, $\dot{\mathbf{x}}$ is the vector of mesh face or edge velocities, and \mathbf{n} is the unit normal of the face or edge. The state vector \mathbf{U} consists of the conserved variables and the Cartesian flux vector $\mathbf{F} = (\mathbf{F}_x, \mathbf{F}_y, \mathbf{F}_z)$ contains both inviscid and viscous fluxes. The equations are closed with the perfect gas equation of state and the Spalart-Allmaras turbulent eddy viscosity model (Ref. 26) for all cases presented in this work. The time derivative term is discretized using a second-order accurate backward-difference formula (BDF2) scheme and the implicit residual is solved using Newton's method. The Jacobian matrix is inverted iteratively using a line-implicit agglomeration multigrid scheme that can also be used as a preconditioner for a GMRES Krylov solver (Ref. 27). For the remainder of this paper, the system of non-linear equations for the computational fluid dynamics (CFD) analysis problem will be represented by the generalized notation:

$$\mathbf{R}(\mathbf{U}, \mathbf{x}) = 0 \quad (3)$$

where the vector \mathbf{U} denotes the flow values and Equation (3) denotes the simultaneous solution of all time steps.

Structural Dynamics Formulation

The rotor blade structure is modeled by a non-linear bend-twist beam model, which is a suitable and widely utilized structural model for slender fixed and rotary wing aircraft structures within the context of an aeroelastic problem. The beam model has been developed previously and coupled to the NSU3D unstructured mesh Reynolds-averaged Navier-Stokes solver (Refs. 28,29). The non-linear governing equations of a slender beam are discretized using the Finite-element method (FEM) in space. Figure 1 shows a typical beam with 15 degrees of freedom for each element to accommodate bend wise,

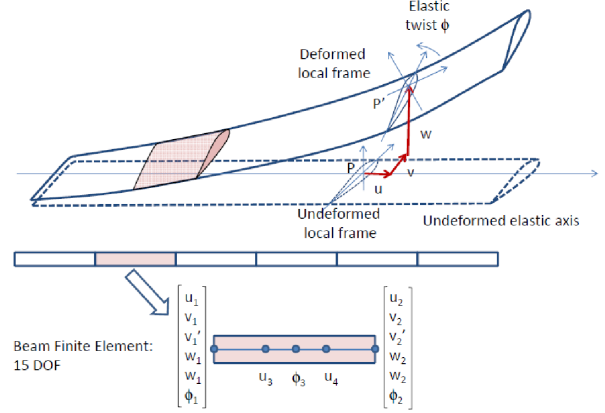


Fig. 1: Beam element with flap, lag, torsional and axial (total 15) degrees of freedom.

Table 1: Comparison of HART-II natural frequencies (Ref. 33)

Modes	Present model	UMARC	DLR
Flap 1	1.104	1.112	1.124
Flap 2	2.802	2.843	2.835
Flap 3	5.010	5.189	5.168
Torsion 1	3.878	3.844	3.845

lag wise, axial and torsional displacements. The second order equation of motion for the beam can be expressed as: $M\ddot{q} + C\dot{q} + Kq = F$, where $[M]$, $[C]$ and $[K]$ are mass, damping and stiffness matrices of the system of equations representing the beam. $F = F(t)$ is the aerodynamic forcing vector and q represents the displacements along all degrees of freedom of the beam. This set of equations can be reduced to a first-order system and solved using a second-order backward difference formula (BDF2) time integration with standard Newton-type linearization and sub-iterations to efficiently invert the implicit system: $[I]\dot{Q} + [A]Q = F$, where $[I]$ is the identity matrix, $Q = [q, \dot{q}]^T$, $F = [0, [M]^{-1}F]^T$ and $[A] = \begin{bmatrix} 0 & -[I] \\ [M]^{-1}[K] & [M]^{-1}[C] \end{bmatrix}$. The residual of the structural equations can be defined as: $J = [I]\dot{Q} + [A]Q - F = 0$, and can be expressed in a simplified form as:

$$\mathbf{J}(\mathbf{Q}, \mathbf{F}) = 0 \quad (4)$$

The beam model consists of 20 elements per blade and has been validated for the standard Hart-2 rotor case (Ref. 30) by comparing its natural frequency predictions with the predictions from other reliable computational structural dynamics (CSD) models, such as UMARC (Ref. 31) and DLR (Ref. 32), as shown in Table 1.

Mesh deformation capability

In order to deform the CFD mesh in response to surface displacements generated by the solution of the CSD beam model,

by cyclic pitching of the rotor blades, and due to blade design shape changes, a linear elastic analogy mesh deformation approach has been implemented. In this approach, the CFD mesh is modeled as a linear elastic solid with a variable modulus of elasticity that can be prescribed either as inversely proportional to cell volume or to the distance of each cell from the nearest wall (Refs. 28,34). The resulting equations are discretized and solved on the mesh in its original undeformed configuration in response to surface displacements using a line-implicit multigrid algorithm analogous to that used for the flow equations. The governing equations for mesh deformation can be written symbolically as:

$$\mathbf{G}(\mathbf{x}, \mathbf{D}) = \mathbf{0} \quad (5)$$

where \mathbf{x} denotes the interior mesh coordinates and \mathbf{D} denotes shape parameters that define the surface geometry.

Prescribed Blade Motion

The time-dependent simulation of a rotor in forward flight requires a prescribed blade motion capability, in particular the individual blade cycling pitching motion must be superimposed with a simple solid body rotation of the entire rotor blade system and CFD mesh that contains the rotor. For each blade, the time-dependent pitch angle can be represented by a combination of mean pitch angle and several harmonic components:

$$\theta = \theta_0 + \sum_{i=1}^n \theta_{c_i} \cos(i\psi) + \sum_{i=1}^n \theta_{s_i} \sin(i\psi) \quad (6)$$

where ψ is the rotor azimuth. We use only one harmonic to attain the required thrust and moments values, hence $i = 1$, and the control parameters $\mathbf{D}_{\text{pitch}} = [\theta_0, \theta_{1c}, \theta_{1s}]$ are to be chosen such that the rotor is trimmed, where θ_0 is the collective and θ_{1c}, θ_{1s} are the two cyclic pitch parameters.

To incorporate rotor pitch actuation three additional equations need to be considered:

- a pitch actuation equation

$$\mathbf{S}^\theta(\mathbf{x}_{s\theta}, \mathbf{x}) = \mathbf{x}_{s\theta} - [\mathbf{T}^\theta(\theta(\mathbf{D}))]\mathbf{x} = \mathbf{0} \quad (7)$$

- a mesh motion equation to propagate surface displacements due to pitch to the interior mesh

$$\mathbf{G}(\mathbf{x}_\theta, \mathbf{x}_{s\theta}) = \mathbf{0} \quad (8)$$

- an azimuthal mesh rotation equation

$$\mathbf{S}^\psi(\mathbf{x}_p, \mathbf{x}_\theta) = \mathbf{x}_p - [\mathbf{T}^\psi]\mathbf{x}_\theta = \mathbf{0} \quad (9)$$

Here $\mathbf{x}_{s\theta}$ denotes the surface mesh coordinates after pitch and \mathbf{x}_θ denotes the interior mesh coordinates after mesh deformation due to pitch, while \mathbf{x}_p denotes the interior mesh point coordinates after rotation. $[\mathbf{T}^\theta]$ and $[\mathbf{T}^\psi]$ are matrix representations for pitch actuation and rotation, respectively.

ACOUSTIC FORMULATION

Despite the continuous increase in computational resources, numerical simulations that resolve wave propagation from the nearfield to a farfield observer are still impractical, hence a viable approach to predicting farfield noise level is the use of hybrid methods that have been developed over the years (Ref. 35) and are now fairly well established.

In hybrid methods the finely resolved nearfield flow time history is used as input to an acoustic formulation that predicts the noise radiated to a given observer. The acoustic formulations are often based on Lighthill's acoustic analogy, in particular the Ffowcs Williams-Hawkings (FW-H) approach, which is the one used in this work (Ref. 36).

Here the NSU3D CFD flow solver provides the nearfield flow time history to a newly developed FW-H acoustic integration module that propagates the acoustic pressure at a farfield observer. A schematic of the hybrid approach is shown in Figure 2(a). The location of the FW-H acoustic integration surface depends on the noise problem being investigated. When significant non-linear flow effects are present, as in the case of high speed helicopter forward flight, an off-body permeable integration surface should be used (Refs. 35, 37). Noise prediction with an off-body permeable surface is only accurate when the flow field between the body and the integration surface is finely resolved, resulting in a significant increase in the computational cost of the CFD time-integration process. However, the case considered in this work consists of a HART-II (Ref. 30) four-bladed rotor in forward flight with a freestream mach number 0.095 and a tip Mach number of 0.638. At these conditions nonlinear flow effects are expected to be negligible so that an on-body impermeable integration surface can be used. Figure 2(b) shows the FW-H acoustic integration surface and the observer location used for validation purposes. The acoustic surface coincides with the CFD rotor surface mesh and every node on the surface is an acoustic source that produces an acoustic pressure at the observer location via the FW-H integration process.

Acoustic Analysis Formulation: the FW-H equation The FW-H equation can be expressed in differential form as (Ref. 35)

$$\left(\frac{\partial^2}{\partial t^2} - c_0^2 \frac{\partial^2}{\partial x_i \partial x_j} \right) (H(f)\rho') = -\frac{\partial F_i \delta(f)}{\partial x_i} + \frac{\partial Q \delta(f)}{\partial t} \quad (10)$$

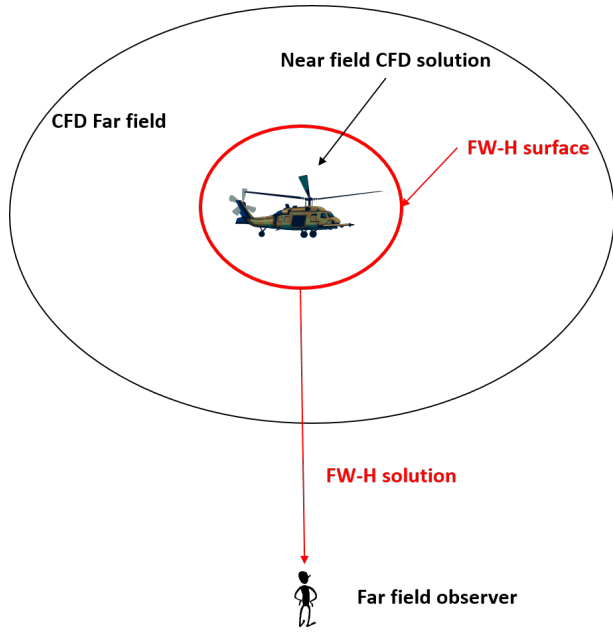
where

$$Q = (\rho_o v_i + \rho(u_i - v_i)) \frac{\partial f}{\partial x_i} \quad (11)$$

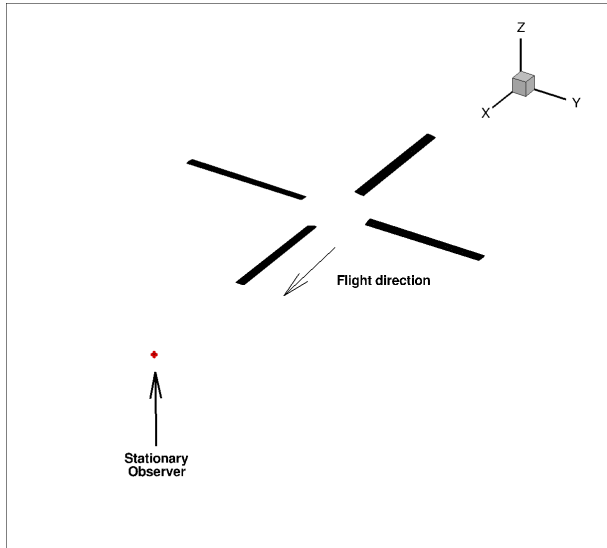
and

$$F_i = (p \delta_{ij} + \rho u_i (u_j - v_j)) \frac{\partial f}{\partial x_j} \quad (12)$$

and the Lighthill's stress tensor, the quadrupole term, has been omitted since it is not used in this work. Equation (11) gives



(a) Schematic of the hybrid approach for the aeroacoustic computation



(b) Acoustic integration surface and observer location

Fig. 2: Schematics of the hybrid acoustic approach (a) and acoustic problem formulation (b): the observer is stationary in the plane of the rotor two radii from the rotor hub at $\psi = 180$ deg.

rise to an unsteady monopole-type contribution that can be associated with mass addition, while the dipole term, equation (12), involves an unsteady force. The function $f(x_i, t) = 0$ defines the surface of integration outside of which the solution is sought. Total density and pressure are ρ and p respectively, the fluid velocities are u_i , while v_i are the surface velocities and c_o is the freestream speed of sound. The prime denotes perturbation relative to the freestream which itself is denoted with the subscript o . x_i and t are Cartesian coordinates and time respectively. $H(f)$ is the Heaviside function while $\delta(f)$ is the Dirac function. A time domain solution to equation (10) can be obtained from the derivation of Farassat (Ref. 38) using

the variables

$$\begin{aligned} U_i &= \left(1 - \frac{\rho}{\rho_o}\right) v_i + \frac{\rho u_i}{\rho_o} \\ L_i &= p' n_j + \rho u_i (u_n - v_n) \end{aligned} \quad (13)$$

as proposed by Di Francescantonio (Ref. 39), where $p' = p - p_o$, $u_n = u_i n_i$, $v_n = v_i n_i$ and n_i is the unit normal of the acoustic surface. The integral solution is then given, neglecting the quadrupole term, by equation (14)

$$\begin{aligned} 4\pi p'_T(\mathbf{y}, t) &= \int_{f=0} \left[\frac{\rho_o (\dot{U}_n + U_n)}{r(1-M_r)^2} \right]_{ret} dS \\ &+ \int_{f=0} \left[\frac{\rho_o U_n K}{r^2(1-M_r)^3} \right]_{ret} dS \\ 4\pi p'_L &= \frac{1}{c_o} \int_{f=0} \left[\frac{\dot{L}_r}{r(1-M_r)^2} \right]_{ret} dS \\ &+ \int_{f=0} \left[\frac{L_r - L_M}{r^2(1-M_r)^2} \right]_{ret} dS \\ &+ \frac{1}{c_o} \int_{f=0} \left[\frac{L_r K}{r^2(1-M_r)^3} \right]_{ret} dS \\ 4\pi p'(\mathbf{y}, t) &= 4\pi p'_T(\mathbf{y}, t) + 4\pi p'_L(\mathbf{y}, t) \end{aligned} \quad (14)$$

where \mathbf{y} is the observer location, t is the observer time, r is the distance between the source \mathbf{x} and the observer \mathbf{y} , M is the surface Mach number and

$$\begin{aligned} U_n &= U_i n_i \\ M_r &= M_i r_i \\ L_r &= L_i r_i \\ L_M &= L_i M_i \\ K &= r \dot{M}_r + c_o (M_r - M^2) \end{aligned} \quad (15)$$

Equation (14) requires the evaluation of the integrals at the emission or retarded time τ : for a given observer location \mathbf{y} and time t the retarded time must be computed via the solution of the nonlinear equation (16)

$$\tau = t - r(\mathbf{x}(\tau), \mathbf{y}(t))/c_o \quad (16)$$

where $r(\mathbf{x}(\tau), \mathbf{y}(t))$ is the distance between the source \mathbf{x} at the emission time τ and the observer \mathbf{y} at the observer time t . This approach has been followed in most acoustic-analogy-based codes (Ref. 35). However, by regarding the source time as the primary time one can choose the source time for an acoustic source and determine when the signal will reach the observer using equation (17)

$$t = \tau + r(\mathbf{x}(\tau), \mathbf{y}(t))/c_o \quad (17)$$

where τ is again the source time and t is the reception time, i.e. the time at which the acoustic disturbance reaches the observer. Equation (17), a rearrangement of equation (16), is easier to solve than its retarded time counterpart as

the observer motion is usually simpler than the motion of the acoustic integration surface. For each acoustic source a sequence of uniformly spaced source times leads to a sequence of unequally spaced observer times as each source has a different source-to-observer distance, hence the acoustic pressure time history for each source must be interpolated at the desired observer time to determine the final acoustic pressure at the observer location. A comparison of the retarded time and the source-time-dominant algorithm is given in (Ref. 40).

In this work we follow this so-called source-time-dominant algorithm as it allows a seamless integration of the acoustic module with the CFD solver. The source time is the CFD time and the integrals in equation (14) are evaluated at every time step during the CFD time integration process. The acoustic integration surface corresponds to the rotor's unstructured surface mesh and each node of the CFD grid corresponds to an acoustic source. All the time derivative terms in equation (14) are approximated with a BDF2 time discretization for consistency with the CFD time integration with the exception of the source acceleration term that is approximated with a second order accurate central difference scheme. The final observer pressure time history is built via linear interpolation of each source time history at the desired observer time after the CFD integration process is completed. The observer acoustic pressure time history can finally be processed to compute the aeroacoustic objective to be minimized. The aeroacoustic objective used in this work is the root mean square of the acoustic pressure time history

$$L_{FWH} = p'_{RMS} = \sqrt{\frac{\sum_{i=1}^{N_{sample}} p'^2(\mathbf{D})}{N_{sample}}} \quad (18)$$

where N_{sample} is the number of samples in the observer acoustic pressure time history and \mathbf{D} is the vector of design variables. The current implementation of the FW-H integral equation has been validated against the PSU-WOPWOP (Ref. 40) acoustic code for the HART-II flexible rotor in trimmed forward flight as shown in Figure 3. The rotor has a freestream Mach number of $M = 0.095$ with a tip Mach number of $M_{tip} = 0.638$, a shaft angle $\alpha_{shaft} = 5.4 \text{ deg}$ and a Reynolds Number of 2 million. The corresponding rotor rotational speed is $\Omega = 1041 \text{ RPM}$ (advance ratio $\mu = 0.15$). The CFD simulation has been carried out for two rotor revolutions on a mesh consisting of approximately 2.32 millions nodes with a 2-degree timestep, 6 CFD/CSD coupling iterations per time step and a stationary in-plane observer located two radii from the rotor hub at an azimuthal angle $\psi = 180 \text{ deg}$ as shown in Figure 2(b) and described in Table 2. Two different observer time windows are shown in Figure 3: an extended time window, Figure 3(a), and the observer time window targeted during the optimization, Figure 3(b). In both cases agreement between the new FW-H implementation and the legacy PSU-WOPWOP code (Ref. 40) is excellent. In Figure 4 we investigate the effect that blade flexibility has on the predicted total acoustic pressure: the positive pressure peak is more pronounced in the flexible case while the negative pressure peak

Table 2: Observer location for the acoustic objective function with respect to the rotor hub, R being the rotor radius

x	y	z
$2R$	0	0

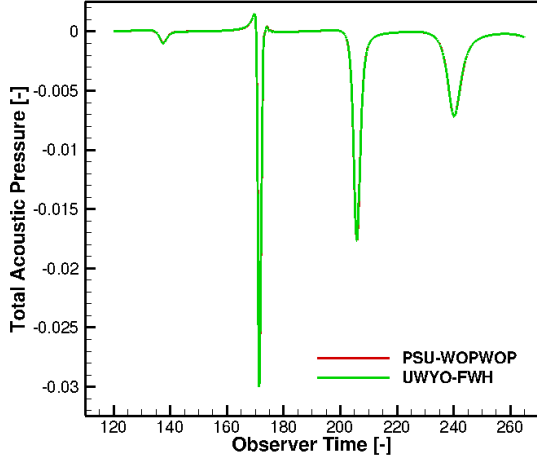
is significantly reduced as a consequence of blade deformation. A comparison of the rigid and flexible blades is shown in Figure 5 together with a surface contour plot of the pressure coefficient. All four blades show different deformation characteristics due to the corresponding different aerodynamic environment they experience during trimmed forward flight: the largest flap displacement is attained at $\psi = 180 \text{ deg}$ while the smallest happens at $\psi = 0 \text{ deg}$.

General solution procedure

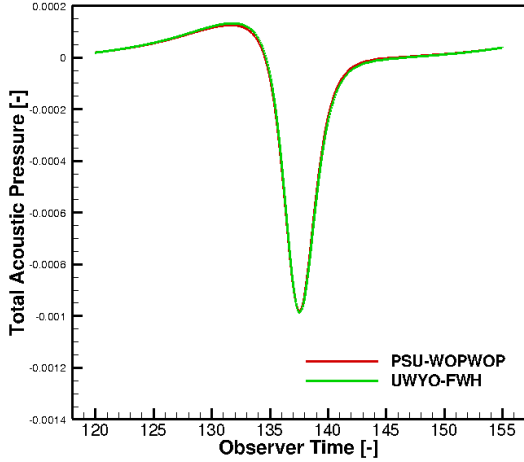
The flexible aeroacoustic problem consists of multiple coupled equations namely, the mesh deformation equations, the flow equations (CFD), the beam model-based structural equations, the fluid-structure interface (FSI) transfer equations, the prescribed blade motion and the acoustic propagation equations. The coupled system of equations to be solved at each time step can be written as:

$$\begin{aligned} \mathbf{G}(\mathbf{x}, \mathbf{D}) &= \mathbf{0} \\ \mathbf{S}^\theta(\mathbf{x}_{s\theta}, \mathbf{x}_s, \mathbf{D}) &= \mathbf{0} \\ \mathbf{G}(\mathbf{x}_\theta, \mathbf{x}_{s\theta}(\mathbf{Q}, \mathbf{D})) &= \mathbf{0} \\ \mathbf{S}^\Psi(\mathbf{x}_p, \mathbf{x}_\theta) &= \mathbf{0} \\ \mathbf{R}(\mathbf{u}, \mathbf{x}_p) &= \mathbf{0} \\ \mathbf{S}(\mathbf{F}_B, \mathbf{Q}, \mathbf{F}(\mathbf{x}_p, \mathbf{u})) &= \mathbf{0} \\ \mathbf{J}(\mathbf{Q}, \mathbf{F}_B) &= \mathbf{0} \\ \mathbf{S}'(\mathbf{x}_s, \mathbf{Q}) &= \mathbf{0} \end{aligned} \quad (19)$$

where $\mathbf{R}(\mathbf{u}, \mathbf{x}_p) = \mathbf{0}$ represents the residual of the flow equations, \mathbf{S} and \mathbf{S}' represent the residuals of the FSI equations, \mathbf{J} represents the residual of the structural analysis problem and the mesh motion residual now depends also on any surface deflections \mathbf{x}_s introduced by the structural model, the displacements arising from the cyclic pitching and the design shape changes. Within each physical time step, solution of the fully coupled fluid structure system of equations consists of performing multiple coupling iterations on each discipline using the latest available values from the other disciplines. Hence, for the current coupling iteration the aerodynamic solver computes pointwise surface forces that are input to the structural model via the FSI procedure. The structural model returns surface structural displacements that are combined with displacements due to blade pitch actuation and fed back into the mesh deformation equations. The entire procedure is then repeated until convergence is obtained for the fully coupled aerostructural problem at the given timestep as shown in Figure 6. At the end of each timestep the latest pressure and



(a) Validation of the current FW-H implementation with the PSU-WOPWOP acoustic code over an extended observer time window.



(b) Comparison between the current FW-H implementation and PSU-WOPWOP over the observer time window used for optimization purposes

Fig. 3: Validation of the current FW-H implementation over an extended (a) and the optimization (b) time window

blade surface information is sent to the FW-H acoustic propagation module to perform the acoustic integration in equation (14), following an approach similar to that of Dunn and Farassat (Ref. 5). After the last timestep the total acoustic pressure time history at the observer is computed via the linear time interpolation procedure described in the previous section.

SENSITIVITY ANALYSIS FOR FLEXIBLE AEROACOUSTIC PROBLEM

For gradient-based optimization, sensitivities of the objective with respect to the design parameters are required. Since the number of design variables is generally very large, an adjoint procedure is used to compute these sensitivities in an efficient

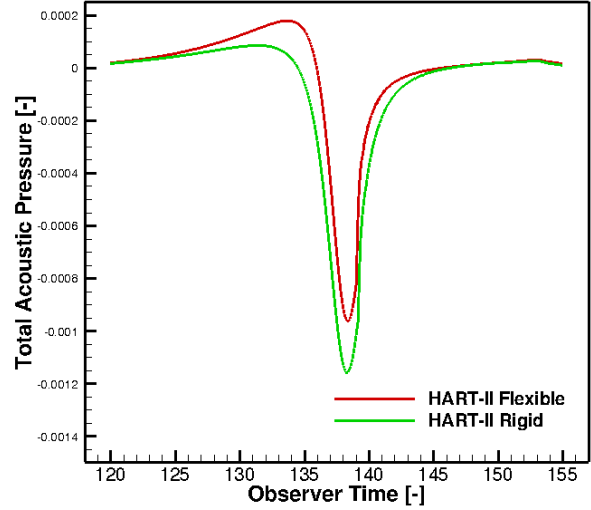


Fig. 4: Acoustic pressure at the observer for the baseline rigid and flexible HART-II rotor.

manner. While a forward or tangent linearization of the analysis problem scales linearly with the number of design variables, the cost of the adjoint or reverse calculation is virtually independent of the number of design parameters. Both tangent and adjoint sensitivity approaches have been implemented in this work by hand differentiation of the flexible aeroacoustic analysis problem. The tangent sensitivity is verified by comparison with the complex-step method (Ref. 41) while the adjoint linearization is verified using the duality relation (Ref. 25) to the tangent approach. Upon verification of the adjoint linearization, the adjoint approach is used in all optimizations.

A schematic of the fully coupled analysis, tangent and adjoint formulation is shown in Figure 7. To derive the tangent linearization we start by expressing any objective functional as

$$L = L(\mathbf{U}(\mathbf{D}), \mathbf{x}(\mathbf{D})) \quad (20)$$

where $\mathbf{U}(\mathbf{D})$ and $\mathbf{x}(\mathbf{D})$ are the aeroelastically converged flow and mesh solution at every time step respectively. Linearization of equation (20) with respect to one design variable gives

$$\frac{dL}{d\mathbf{D}} = \begin{bmatrix} \frac{\partial L}{\partial \mathbf{x}} & \frac{\partial L}{\partial \mathbf{U}} \end{bmatrix} \begin{bmatrix} \frac{d\mathbf{x}}{d\mathbf{D}} \\ \frac{d\mathbf{U}}{d\mathbf{D}} \end{bmatrix} \quad (21)$$

Differentiation of the system of equations (19) yields the system of equations (22) which represent the tangent sensitivity

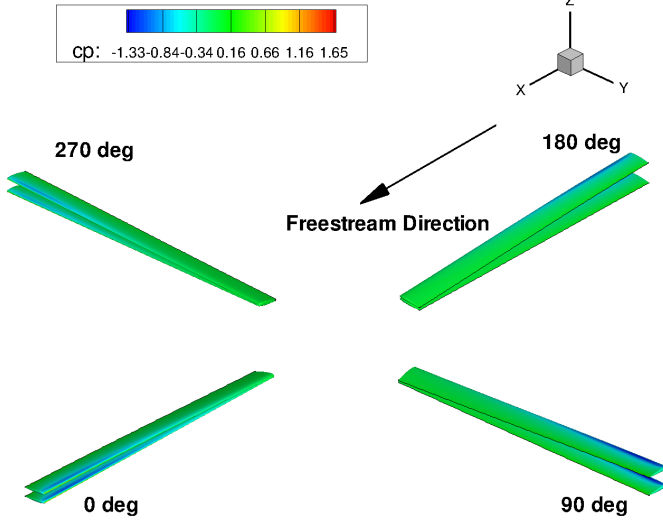


Fig. 5: Comparison between the rigid and the flexible HART-II rotor.

of the fully coupled aeroelastic problem.

$$\begin{bmatrix}
 \frac{\partial G}{\partial \mathbf{x}} & 0 & 0 & 0 & 0 & 0 & 0 & 0 \\
 \frac{\partial S^\theta}{\partial \mathbf{x}} & \frac{\partial S^\theta}{\partial x_{S\theta}} & 0 & 0 & 0 & 0 & 0 & \frac{\partial S^\theta}{\partial x_S} \\
 0 & \frac{\partial G}{\partial x_{S\theta}} & \frac{\partial G}{\partial x_\theta} & 0 & 0 & 0 & 0 & 0 \\
 0 & 0 & \frac{\partial S^w}{\partial x_\theta} & \frac{\partial S^w}{\partial x_p} & 0 & 0 & 0 & 0 \\
 0 & 0 & 0 & \frac{\partial R}{\partial x_p} & \frac{\partial R}{\partial \mathbf{u}} & 0 & 0 & 0 \\
 0 & 0 & 0 & \frac{\partial S}{\partial x_p} & \frac{\partial S}{\partial \mathbf{u}} & \frac{\partial S}{\partial \mathbf{F}_b} & 0 & 0 \\
 0 & 0 & 0 & 0 & 0 & \frac{\partial J}{\partial \mathbf{F}_b} & \frac{\partial J}{\partial Q} & 0 \\
 0 & 0 & 0 & 0 & 0 & 0 & \frac{\partial S'}{\partial Q} & \frac{\partial S'}{\partial x_S}
 \end{bmatrix}$$

$$\begin{bmatrix}
 \frac{d\mathbf{x}}{d\mathbf{D}} \\
 \frac{dx_{S\theta}}{d\mathbf{D}} \\
 \frac{dx_\theta}{d\mathbf{D}} \\
 \frac{dx_p}{d\mathbf{D}} \\
 \frac{d\mathbf{U}}{d\mathbf{D}} \\
 \frac{d\mathbf{F}_b}{d\mathbf{D}} \\
 \frac{dQ}{d\mathbf{D}} \\
 \frac{dx_S}{d\mathbf{D}}
 \end{bmatrix}
 \times
 \begin{bmatrix}
 -\frac{\partial G}{\partial \mathbf{D}} \\
 -\frac{\partial S^\theta}{\partial \mathbf{D}} \\
 0 \\
 0 \\
 0 \\
 0 \\
 0 \\
 0
 \end{bmatrix}
 =
 \begin{bmatrix}
 \frac{d\mathbf{x}}{d\mathbf{D}} \\
 \frac{dx_{S\theta}}{d\mathbf{D}} \\
 \frac{dx_\theta}{d\mathbf{D}} \\
 \frac{dx_p}{d\mathbf{D}} \\
 \frac{d\mathbf{U}}{d\mathbf{D}} \\
 \frac{d\mathbf{F}_b}{d\mathbf{D}} \\
 \frac{dQ}{d\mathbf{D}} \\
 \frac{dx_S}{d\mathbf{D}}
 \end{bmatrix}
 \quad (22)$$

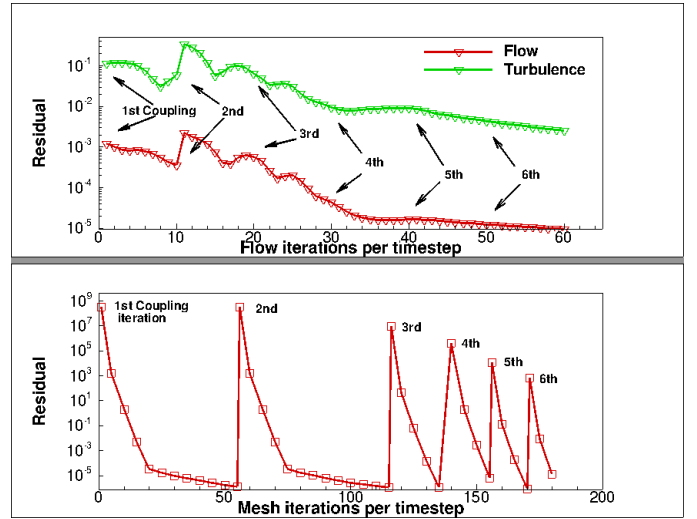


Fig. 6: Flow and mesh residual at a generic timestep highlighting the aeroelastic coupling procedure. Flow and mesh data at the end of each timestep are then used to determine the noise signature by evaluation of the acoustic integrals.

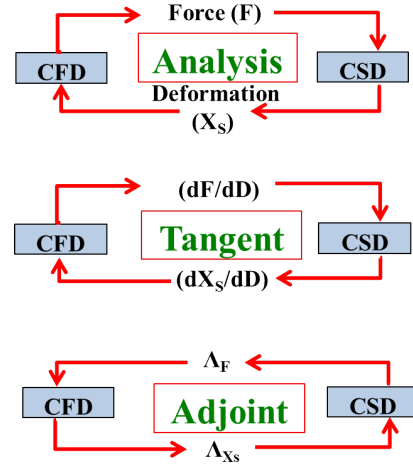


Fig. 7: Illustration of information flow for aerostructural analysis, forward sensitivity and adjoint formulations

The system in equation (22) represent a forward integration in time the solutions of which are the flow and mesh tangent sensitivities $\frac{d\mathbf{U}}{d\mathbf{D}}$ and $\frac{d\mathbf{x}}{d\mathbf{D}}$ respectively that can be used to compute the objective functional sensitivity in equation (21), as detailed in (Ref. 42). In the case of an acoustic objective, the flow and mesh tangent sensitivities $\frac{d\mathbf{U}}{d\mathbf{D}}$ and $\frac{d\mathbf{x}}{d\mathbf{D}}$ are passed to the forward linearization of the FW-H equation to determine the sensitivity of the acoustic objective functional in equation (18) as detailed in the next section. The aeroelastic adjoint formulation can be obtained by transposing the tangent lin-

earization in equation (22), resulting in equation (23).

$$\begin{bmatrix}
\frac{\partial \mathbf{G}^T}{\partial \mathbf{x}} & \frac{\partial \mathbf{S}^{\theta T}}{\partial \mathbf{x}} & 0 & 0 & 0 & 0 & 0 & 0 \\
0 & \frac{\partial \mathbf{S}^{\theta T}}{\partial \mathbf{x}_{s\theta}} & \frac{\partial \mathbf{G}^T}{\partial \mathbf{x}_{s\theta}} & 0 & 0 & 0 & 0 & 0 \\
0 & 0 & \frac{\partial \mathbf{G}^T}{\partial \mathbf{x}_\theta} & \frac{\partial \mathbf{S}^{\psi T}}{\partial \mathbf{x}_\theta} & 0 & 0 & 0 & 0 \\
0 & 0 & 0 & \frac{\partial \mathbf{S}^{\psi T}}{\partial \mathbf{x}_p} & \frac{\partial \mathbf{R}^T}{\partial \mathbf{x}_p} & \frac{\partial \mathbf{S}'^T}{\partial \mathbf{x}_p} & 0 & 0 \\
0 & 0 & 0 & 0 & 0 & \frac{\partial \mathbf{S}'^T}{\partial \mathbf{F}_b} & \frac{\partial \mathbf{J}^T}{\partial \mathbf{F}_b} & 0 \\
0 & 0 & 0 & 0 & 0 & 0 & \frac{\partial \mathbf{J}^T}{\partial \mathbf{Q}} & \frac{\partial \mathbf{S}'^T}{\partial \mathbf{Q}} \\
0 & \frac{\partial \mathbf{S}^{\theta T}}{\partial \mathbf{x}_s} & 0 & 0 & 0 & 0 & 0 & \frac{\partial \mathbf{S}'^T}{\partial \mathbf{x}_s}
\end{bmatrix}
\times
\begin{bmatrix}
\Lambda_{\mathbf{x}} \\
\Lambda_{\mathbf{x}_{s\theta}} \\
\Lambda_{\mathbf{x}_\theta} \\
\Lambda_{\mathbf{u}} \\
\Lambda_{\mathbf{F}_b} \\
\Lambda_{\mathbf{Q}} \\
\Lambda_{\mathbf{x}_s}
\end{bmatrix}
=
\begin{bmatrix}
0 \\
0 \\
0 \\
\frac{\partial \mathbf{L}^T}{\partial \mathbf{x}} \\
\frac{\partial \mathbf{L}^T}{\partial \mathbf{u}} \\
0 \\
0 \\
0
\end{bmatrix}
\quad (23)$$

Equation (23) represents an integration backward in time the solutions of which include the flow and mesh adjoint variables $\Lambda_{\mathbf{u}}$ and $\Lambda_{\mathbf{x}}$ used to compute the objective functional sensitivity as

$$\frac{d\mathbf{L}^T}{d\mathbf{D}} = \begin{bmatrix} \frac{\partial \mathbf{G}^T}{\partial \mathbf{D}} & 0 \end{bmatrix} \begin{bmatrix} \Lambda_{\mathbf{x}} \\ \Lambda_{\mathbf{u}} \end{bmatrix} \quad (24)$$

as explained in (Ref. 42). The backward time-integration procedure requires the solution to be written out to disk at each time step in the analysis run, in order that it can be read back in by the adjoint solver as it proceeds backwards in time. In the case of the aeroacoustic objective function in equation (18) the reverse linearization of the FW-H equation provides the right hand side term in equation (23) as detailed below.

Sensitivity formulation for the integral FW-H equation

Computing the sensitivities of the coupled flexible aeroacoustic problem requires the linearization of the acoustic module with respect to the design variables. The sensitivity formulation for the current implementation of the integral FW-H equation closely mimics the linearization of the CFD code as detailed in references (Refs. 24, 25). First the tangent linearization of the acoustic code has been developed by exact hand-differentiation of the discretized integral FW-H equation. The

tangent linearization has then been transposed and applied in reverse order to obtain the adjoint sensitivity with respect to the full vector of design variables.

Tangent sensitivity formulation The tangent linearization of the acoustic objective function allows the computation of the objective function sensitivity with respect to a single design variable. We express the acoustic pressure at the observer location and time as

$$p'(\mathbf{y}, t, \mathbf{D}) = \mathbf{FWH}(\mathbf{U}(\mathbf{D}), \mathbf{x}(\mathbf{D})) \quad (25)$$

where \mathbf{D} is the vector of design variables and $\mathbf{FWH}(\mathbf{U}(\mathbf{D}), \mathbf{x}(\mathbf{D}))$ represents all the discrete operations necessary to evaluate equation (14) numerically. In this expression $\mathbf{U}(\mathbf{D})$ and $\mathbf{x}(\mathbf{D})$ are the flow and mesh solution at every time step of the time-integration process at the acoustic integration surface, after the aeroelastic coupling has converged. The acoustic pressure tangent sensitivity time history can be expressed as

$$\frac{dp'(\mathbf{y}, t, \mathbf{D})}{d\mathbf{D}} = \sum_n \frac{\partial \mathbf{FWH}}{\partial U_{FWH}^n} \frac{dU_{FWH}^n}{d\mathbf{D}} + \frac{\partial \mathbf{FWH}}{\partial x_{FWH}^n} \frac{dx_{FWH}^n}{d\mathbf{D}} \quad (26)$$

so that the tangent linearization of the acoustic objective function p'_{RMS} defined in equation (18) becomes:

$$\begin{aligned}
\frac{dL_{FWH}}{d\mathbf{D}} &= \sum_n \frac{\partial L_{FWH}}{\partial U_{FWH}^n} \frac{dU_{FWH}^n}{d\mathbf{D}} + \frac{\partial L_{FWH}}{\partial x_{FWH}^n} \frac{dx_{FWH}^n}{d\mathbf{D}} \\
&= \frac{\partial p'_{RMS}}{\partial p'} \left[\sum_n \frac{\partial \mathbf{FWH}}{\partial U_{FWH}^n} \frac{dU_{FWH}^n}{d\mathbf{D}} + \frac{\partial \mathbf{FWH}}{\partial x_{FWH}^n} \frac{dx_{FWH}^n}{d\mathbf{D}} \right] \\
&= \frac{\partial p'_{RMS}}{\partial p'} \frac{dp'}{d\mathbf{D}} \quad (27)
\end{aligned}$$

In equation (27) the terms $\frac{dU_{FWH}^n}{d\mathbf{D}}$ and $\frac{dx_{FWH}^n}{d\mathbf{D}}$ are the aeroelastically-converged flow and mesh tangent sensitivities at every time step evaluated at the acoustic integration surface that are computed via the forward time integration described by equation (22). The terms $\frac{\partial \mathbf{FWH}}{\partial U_{FWH}^n}$ and $\frac{\partial \mathbf{FWH}}{\partial x_{FWH}^n}$ are the tangent linearizations of equation (14). The tangent acoustic problem proceeds in analogy with the acoustic analysis problem. The tangent flow solution and the tangent acoustic solution are carried out simultaneously: the aeroelastically-converged tangent flow solution is used to assemble the tangent sensitivities of all the terms in equation (15) which in turn are used to evaluate the tangent sensitivity of the integral equation (14) at every timestep, resulting in an unequally spaced acoustic pressure sensitivity at the observer location for every acoustic source. The final observer acoustic pressure sensitivity time history is built via linearization of the time interpolation algorithm at the end of the time-integration process allowing for the computation of the acoustic objective function sensitivity, equation (27), with respect to one design variable.

Adjoint sensitivity formulation The adjoint sensitivity can be derived by transposing the tangent sensitivity formulation.

Transposing equation (27) yields

$$\begin{aligned} \frac{dL_{FWH}^T}{dD} &= \left[\sum_n \frac{dU_{FWH}^n}{dD} \frac{\partial FWH^T}{\partial U_{FWH}^n} + \frac{dx_{FWH}^n}{dD} \frac{\partial FWH^T}{\partial x_{FWH}^n} \right] \frac{\partial p'_{RMS}}{\partial p}{}^T \\ &= \sum_n \frac{\partial U^n}{\partial D} \frac{\partial L_{FWH}^T}{\partial U^n} + \frac{\partial x^n}{\partial D} \frac{\partial L_{FWH}^T}{\partial x^n} \end{aligned} \quad (28)$$

The terms $\frac{\partial L_{FWH}^T}{\partial U^n} = \frac{\partial FWH^T}{\partial U_{FWH}^n} \frac{\partial p'_{RMS}}{\partial p}{}^T$ and $\frac{\partial L_{FWH}^T}{\partial x^n} = \frac{\partial FWH^T}{\partial x_{FWH}^n} \frac{\partial p'_{RMS}}{\partial p}{}^T$ represent the right-hand-side of equation (23) for the case of the acoustic objective function and drive the adjoint backward time-integration described in equation (23). The term $\frac{\partial p'_{RMS}}{\partial p}{}^T$ is the reverse linearization of the observer time interpolation process that needs to be evaluated before the adjoint time-integration can start while the term $\frac{\partial FWH^T}{\partial U_{FWH}^n}$ and $\frac{\partial FWH^T}{\partial x_{FWH}^n}$ correspond to the reverse linearization of the acoustic integrals in equation (14). At the end of the backward time-integration process, the full sensitivity vector of the acoustic objective function is recovered.

Sensitivity verification The coupled adjoint flexible aeroacoustic sensitivity to be used by the gradient based optimization algorithm is verified with the complex step differentiation method (Ref. 41). Any function $f(x)$ operating on a real variable x can be used to compute both the function and its derivative $f'(x)$ if the input variable x and all the intermediate variables used in the discrete evaluation of $f(x)$ are redefined as complex variables. In this case for a complex input the function will produce a complex output. A Taylor series of the now complex function $f(x + ih)$, where h is a small step-size and i is the imaginary unit, reads

$$f(x + ih) = f(x) + ihf'(x) + O(h^2) \quad (29)$$

from which the real part is simply the function value at x , while from the imaginary part the function derivative can be easily evaluated as

$$f'(x) = \frac{Im[f(x + ih)]}{h} \quad (30)$$

Despite requiring a step size, as in the case of finite-differencing, the complex step method is insensitive to small step-sizes since no differencing is required. This allows the tangent formulation to be verified to machine precision. In this work a step-size of $h = 10^{-31}$ has been used.

For the verification study, two revolutions of the Hart-2 rigid rotor are simulated on a mesh consisting of approximately 107,000 nodes using a 4-degree timestep. The acoustic objective time history is recorded over only the last revolution for the same observer time window as in Figure 3(b) and the sensitivity is computed with respect to the twist of the root section and to the first cyclic pitch parameter. Figure 8 shows excellent agreement between the tangent pressure sensitivity time history, equation (26), and its complex counterpart. Further verification of the acoustic objective function sensitivity

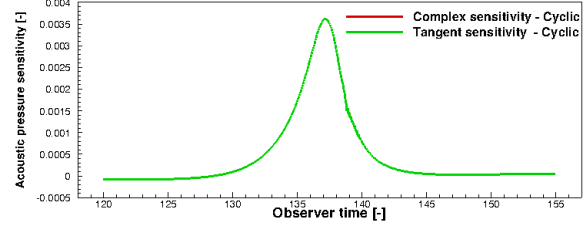
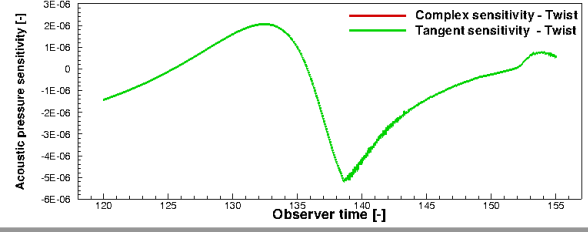


Fig. 8: Complex step verification of the tangent acoustic pressure time history sensitivity

Table 3: Adjoint sensitivity verification for the p'_{RMS} objective function w.r.t. the root twist design variable.

Complex	1.46204808801E-06
Tangent	1.4620480687-06
Adjoint	1.46204808794E-06

Table 4: Adjoint sensitivity verification for the p'_{RMS} objective function w.r.t. the first cyclic design variable.

Complex	-4.269878110954E-04
Tangent	-4.269878110962E-04
Adjoint	-4.269878110854E-04

in equation (27) is shown in Table 3 for the root twist design variable and in Table 4 for the first cyclic pitch parameter. The tangent sensitivity allows for the verification of the adjoint sensitivity by the duality relation (Ref. 25). The current aeroacoustic adjoint implementation is verified by comparing the adjoint sensitivity to the unsteady forward and complex step sensitivities with respect to the twist of the root section, in Table 3, and to the first cyclic pitch parameter, in Table 4. The flow and structural equations are converged to machine precision to avoid any algebraic error, and the complex, tangent and adjoint sensitivities are seen to agree to 9 significant figures. The adjoint sensitivities can then be used in the gradient based optimization process.

RESULTS

The goal of the present work is to reduce the noise signature of the HART-II rotor in trimmed forward flight by means of gradient-based optimization techniques that exploit the multidisciplinary flexible aeroacoustic adjoint method developed so far. As a preliminary step, the flexible HART-II rotor in forward flight needs to be trimmed to establish a starting point for

all subsequent optimizations. The trim problem is formulated as an optimization problem described by equation (31)

$$\begin{aligned}
& \min L_{THRUST} \\
& \text{subject to} \\
& L_{LATERAL} = 0 \\
& \text{w.r.t. } \mathbf{D}_{pitch}
\end{aligned} \tag{31}$$

where the vector of design variables \mathbf{D}_{pitch} is made up of one collective and two cyclics and is described in the ‘‘Prescribed Blade Motion’’ section. One design cycle for this optimization corresponds to one unsteady aeroelastic flow solution and two aeroelastic adjoint solutions, one for the objective and one for the constraint function in equation (31).

Once the Har-II baseline rotor has been trimmed, two different optimizations are performed, following an approach similar to that of Nielsen et al. (Ref. 16). The first aeroacoustic optimization aims at reducing the rotor’s noise signature under the trim constraint only, as shown in equation (32).

$$\begin{aligned}
& \min p'_{RMS} \\
& \text{subject to} \\
& L_{THRUST} = 0 \\
& L_{LATERAL} = 0 \\
& \text{w.r.t. } \mathbf{D}
\end{aligned} \tag{32}$$

In this case one design cycle for this optimization corresponds to one unsteady aeroelastic flow solution and three unsteady aeroelastic adjoint solutions, one adjoint solution for the objective and one adjoint solution for each constraint. The noise signature of the resulting optimum rotor provides a limit of the achievable noise reduction, but it will come at the expense of the rotor’s performance as detailed in the following sections. Hence, the last optimization is a multidisciplinary aeroacoustic optimization and aims at reducing the torque required for trimmed forward flight with a significantly lower noise signature according to equation (33).

$$\begin{aligned}
& \min L_{TORQUE} \\
& \text{subject to} \\
& L_{THRUST} = 0 \\
& L_{LATERAL} = 0 \\
& p'_{RMS} = p'_{RMS_{TARGET}} \\
& \text{w.r.t. } \mathbf{D}
\end{aligned} \tag{33}$$

The value $p'_{RMS_{TARGET}}$ has been chosen to guarantee a 2dB OSPL noise signature reduction of the baseline rotor. In this case one design cycle consists of one aeroelastic unsteady flow solution, and four aeroelastic unsteady adjoint solutions. The functionals L_{THRUST} , $L_{LATERAL}$ and L_{TORQUE} are defined

as

$$\begin{aligned}
L_{THRUST} &= \frac{1}{N} \left(\sum_{i=1}^N (C_T^i - C_{T_{AVERAGE}}^i) \right)^2 \\
L_{LATERAL} &= \frac{1}{N} \left[\left(\sum_{i=1}^N C_{M_x}^i \right)^2 + \left(\sum_{i=1}^N C_{M_y}^i \right)^2 \right] \\
L_{TORQUE} &= \frac{1}{N} \sum_{i=1}^N (C_Q^i)^2
\end{aligned} \tag{34}$$

where $C_{T_{AVERAGE}}^i = 0.0044$ is the target thrust coefficient for the baseline Har-II rotor. The flow conditions are those described previously and the simulations are run for two rotor revolutions using a 2 degree timestep and a computational mesh that consists of approximately 2.32 million nodes. Six CFD/CSD coupling iterations are performed at every time step. The aerodynamic functionals in equation (34) are accumulated only over the second revolution to prevent the optimization algorithm from focusing on the initial transient. The acoustic integration is performed only over the second revolution and the acoustic objective function is evaluated over the observer time window shown in Figure 3(b). For all optimizations the observer is stationary and is placed in front of the rotor as shown in Figure 2(b) and detailed in Table 2.

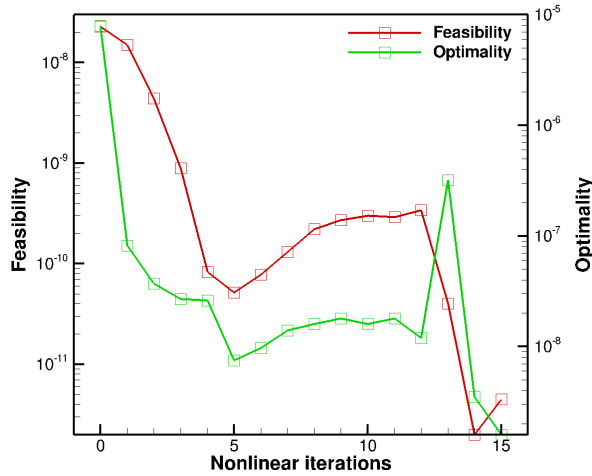
In this work we consider only shape design variables that affect the outer mold line of the CFD geometry without modifying the structural model. The influence of these aerodynamic design variables affects the aeroelastic loop only through changes in the aerodynamic forces applied to the structural model. The baseline blade is constructed by stacking 9 airfoils along the span. Each airfoil is parameterized with 10 Hicks-Henne bump functions, 5 for the upper surface and 5 for the lower surface respectively. Blade twist varies linearly between root and tip, while one collective and two cyclics allow the trimming of the rotor, for a total of 95 design variables in the vector of design variables \mathbf{D} in equation (32) and (33). One unsteady flow solution takes approximately 90 minutes of wall-clock time on 1024 cores with each unsteady adjoint solution costing approximately 45 minutes of wall clock time, so that the cost of one design cycle spans from three hours for the trim optimization, equation (31), to five hours for the aeroacoustic optimization, equation (33). Approximately 650 Gb of disk space are stored to disk during the analysis problem and read in by the flexible aeroacoustic adjoint procedure. The SNOPT (Ref. 43) sequential quadratic programming algorithm is used to drive the constrained optimization. The computational cost of any of the optimizations in equation (32) or (33) is approximately 96 hours of wall-clock time on 1024 cores on the Yellowstone supercomputer at the NCAR-Wyoming Supercomputing Center (NWSC).

We give convergence results for the optimization problems as a function of nonlinear optimization iterations and of design cycles. While the number of design cycles is a measure of the optimization wall-clock time, the number of nonlinear iterations is the number of iterations used by SNOPT to solve the optimization problem; convergence of the optimization is assessed through feasibility, which is a measure of the constraint

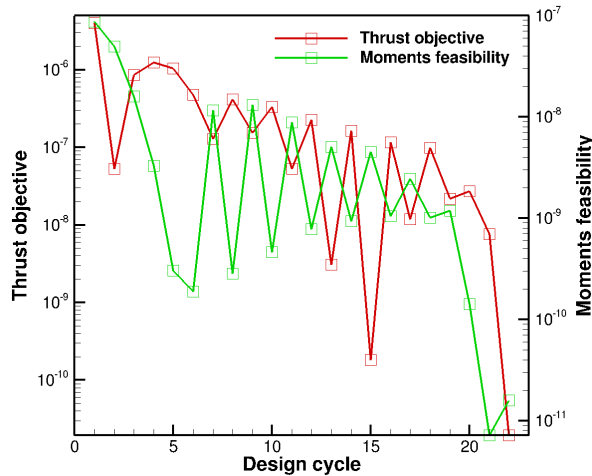
violation, and optimality, which is a measure of the satisfaction of the Karush - Kuhn - Tucker condition as described in (Ref. 43).

Trim results

The trim optimization problem is described by equation (31). The optimization convergence is shown in Figure 9. After



(a) Feasibility and optimality of the trim problem as a function of nonlinear optimization iterations



(b) Convergence of the thrust objective function and moment constraint as a function of design cycles.

Fig. 9: Convergence of the trim optimization problem

15 nonlinear iterations and 22 design cycles the feasibility and optimality of the optimization problem are reduced by approximately 3 orders of magnitude and the baseline flexible HART-II rotor is trimmed as further confirmed by thrust and lateral moments time histories shown in Figure 10. The

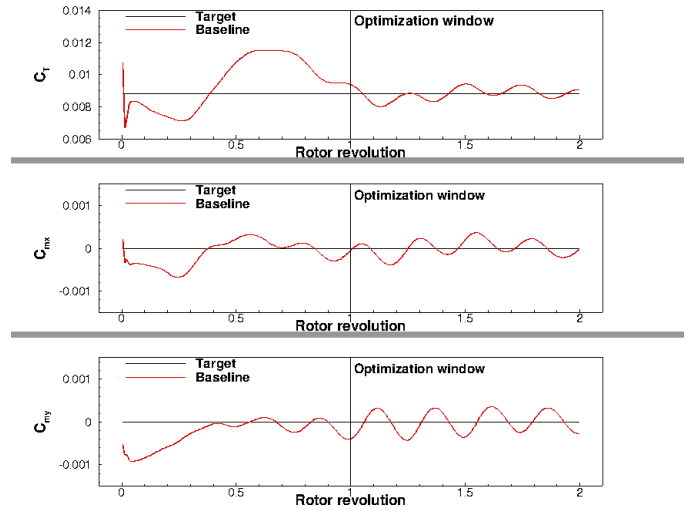


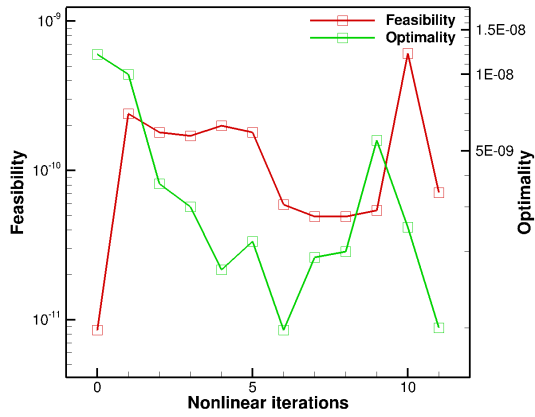
Fig. 10: Thrust and moments time histories for the baseline HART-II rotor

trimmed HART-II rotor will now serve as the initial design for all subsequent aeroacoustic optimizations.

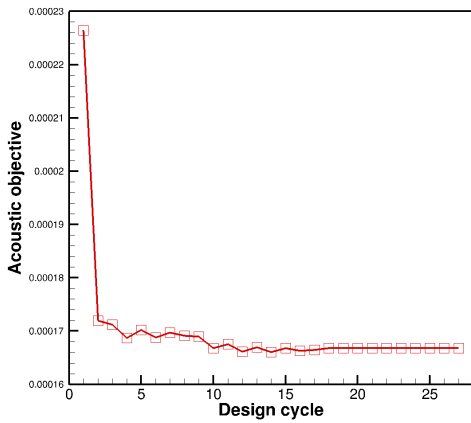
Aeroacoustic optimization

As mentioned above the initial design is the trimmed HART-II rotor from the previous section and the optimization problem is described in equation (32). SNOPT convergence is shown in terms of nonlinear optimization iterations and design cycles in Figure 11. After 27 design cycles the optimization produces a geometry that reduces the Overall Sound Pressure Level of 2.6 dB while keeping the rotor trimmed as highlighted by the thrust and lateral moments time histories shown in Figure 12. The acoustic pressure time history is shown in Figure 13. The main reduction in total acoustic pressure comes from the reduction in thickness noise while the loading pressure minimization is less significant. The noise minimization is achieved with rather thick airfoils especially at the inboard sections, as shown in Figure 14. Blade root cap shape considerations dictate the shape of the most inboard airfoil at the first spanwise station: since we build the blade cap as a surface of revolution that joins the upper and lower surface of the blade, the design variables for the root airfoil needed to be bounded more than the design variables for the other airfoils to guarantee a reasonable blade root cap, resulting in the first airfoil shown in Figure 14. Since rotor torque is not included in the optimization, the noise reduction achieved here, despite representing the maximum noise reduction achievable within the current optimization framework, comes at the expense of rotor performance, as clearly indicated in Figure 15.

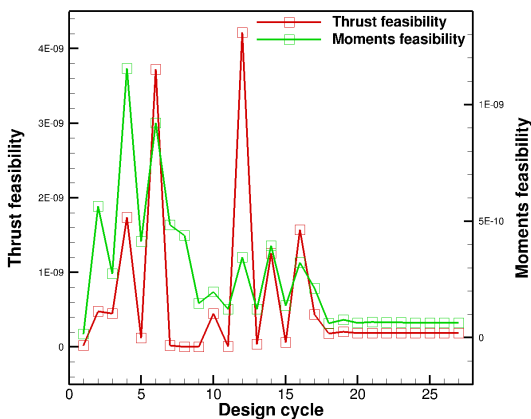
The optimization described by equation (33) and discussed in the next section addresses this issue by minimizing the required torque while constraining the acoustic signature to a lower noise level than the baseline rotor.



(a) Feasibility and optimality for the aeroacoustic optimization problem as a function of nonlinear iterations



(b) Convergence of the aeroacoustic objective function as a function of design cycles.



(c) Convergence of the trim constraint as a function of design cycles.

Fig. 11: Convergence of the aeroacoustic optimization problem

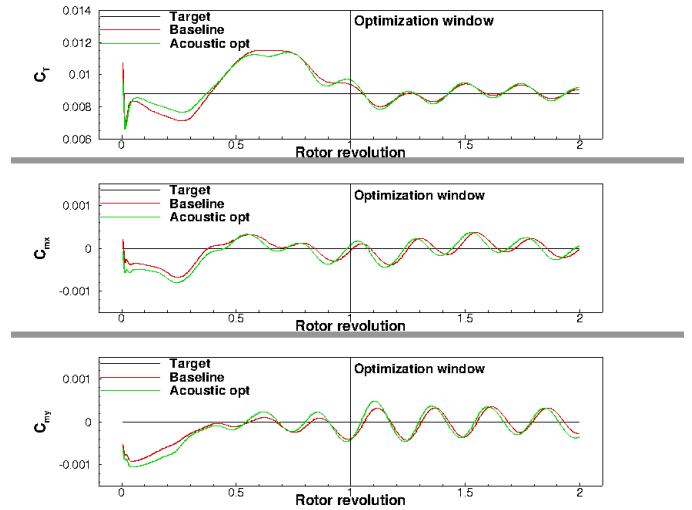


Fig. 12: Thrust and moments time histories for the baseline and optimized HART-II rotor

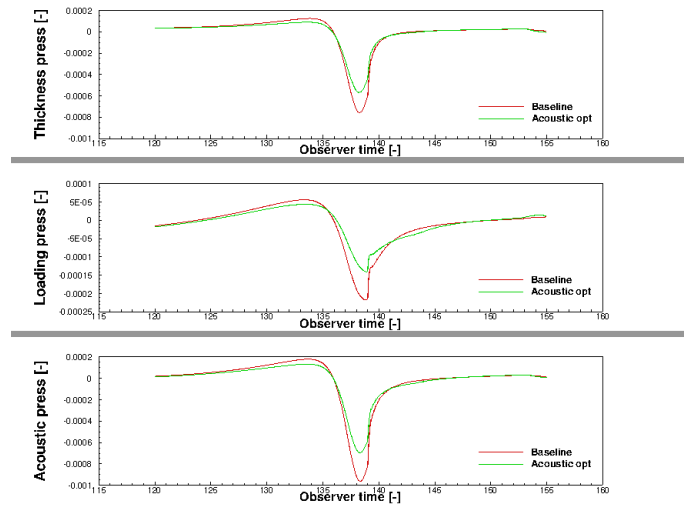


Fig. 13: Thickness, loading and total acoustic pressures at the observer for the aeroacoustically optimized rotor

Acoustically-constrained torque minimization

The initial design for this multidisciplinary aeroacoustic optimization is again the trimmed HART-II rotor and the optimization problem is described in equation (33). In as few as 5 nonlinear iterations feasibility is reduced by more than 2 orders of magnitude while optimality is reduced by approximately 9 orders of magnitude, as shown in Figure 16(a). After 10 design cycles the acoustic constraint is satisfied resulting in a rotor with a 2dB OSPL reduction compared to the baseline, while the required torque is reduced by 2.5% as shown in Figure 16(b). Satisfaction of the trim constraint is shown in Figure 16(c) and confirmed by the thrust and lateral moment time histories shown in Figure 17. A comparison of the torque time histories is shown in Figure 18 highlighting the 2.5% torque reduction achieved for this optimization. The thickness, loading and total acoustic pressure time histories are shown in Figure 19. The thickness acoustic pressure is essentially the same between the current optimization and the one from the previ-

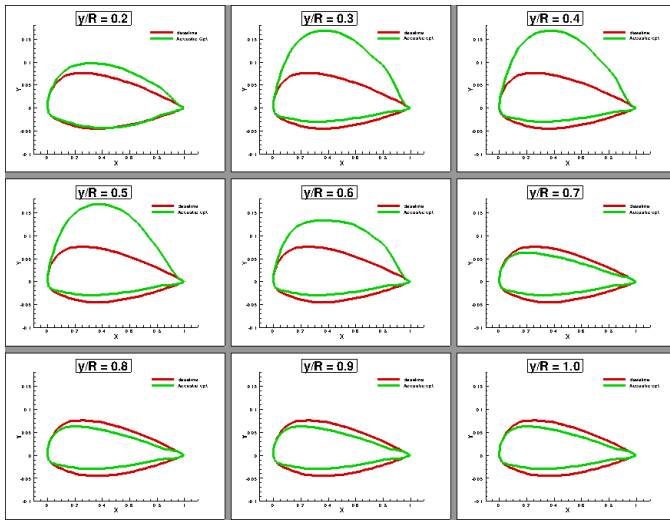


Fig. 14: Baseline (red) and optimized (green) airfoil shapes for the aeroacoustically optimized rotor

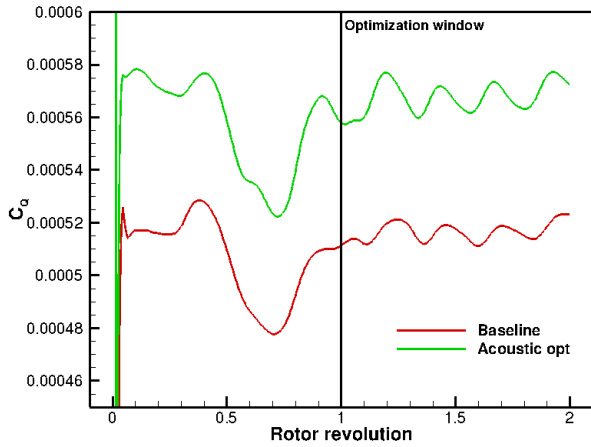
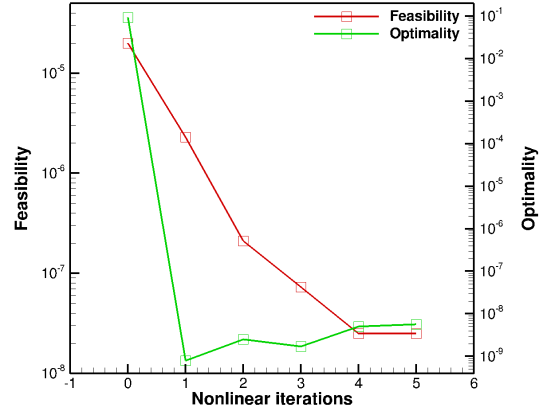


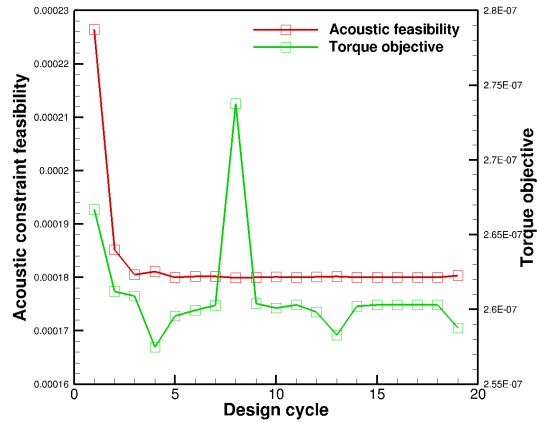
Fig. 15: Torque time history for the baseline and aeroacoustically optimized rotors showing the performance penalty paid to minimize the acoustic signature.

ous section, suggesting that the two minimizations exploit the same noise reduction mechanism, while loading pressure reduction for the current optimization is significantly lower. A comparison of the airfoil shapes for the baseline and the two optimized rotors is shown in Figure 20 highlighting that the acoustically constrained torque minimization results in more conventional blade shapes at the inboard sections while recovering the same airfoils of the aeroacoustic optimization at the outboard sections.

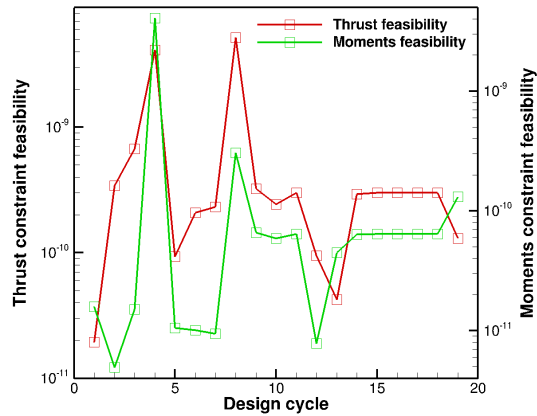
Previous noise mitigation studies (Ref. 3) have shown that optimizing for one observer location can result in higher noise levels at different observer locations. A directivity study for the optimized rotor reveals that the current design is capable of reducing noise at in-plane observer locations that have not been targeted by the optimization as shown for two different observers placed at $\psi = 135$ and $\psi = 315$ degrees as shown in Figure 21.



(a) Feasibility and optimality for the torque-constrained aeroacoustic optimization problem as a function of nonlinear iterations



(b) Convergence of the acoustic objective function and the torque constraint as a function of design cycles.



(c) Convergence of the trim feasibility as a function of design cycles.

Fig. 16: Convergence of the acoustically constrained torque optimization

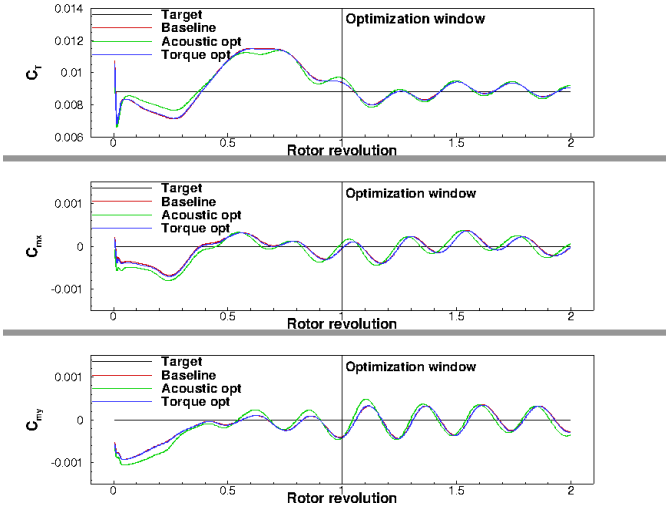


Fig. 17: Thrust and moments time histories for the baseline rotor, the aeroacoustic optimized rotor and the acoustically constrained torque optimized rotor

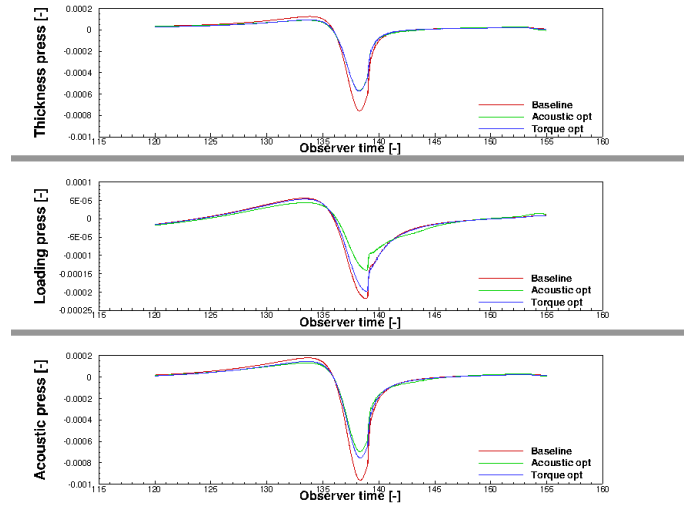


Fig. 19: Thickness, loading and total acoustic pressures at the observer for the acoustically constrained torque optimized rotor.

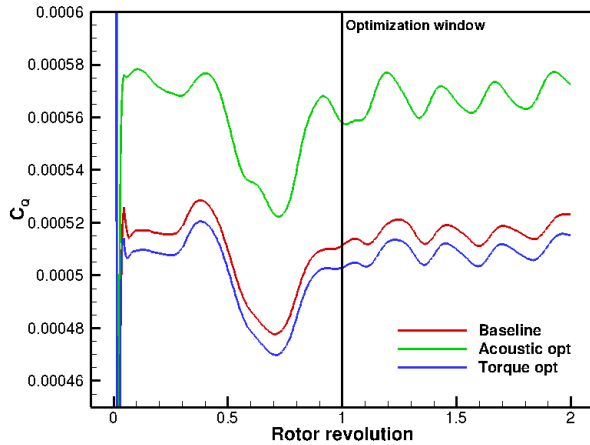


Fig. 18: Torque time histories for for the baseline rotor, the aeroacoustic optimized rotor and the acoustically constrained torque optimized rotor

OPTIMIZATION RESULTS VALIDATION OVER MULTIPLE ROTOR REVOLUTIONS

In this section we investigate the behavior of the baseline and the optimized rotors from the previous sections when their performance is evaluated over multiple rotor revolutions. While the previous computations have been run for only 2 rotor revolutions, the current simulations have been run for four rotor revolutions and the aerodynamic objective functions are accumulated over the last 3 revolutions. The acoustic objective function is evaluated over the same observer time window as in the previous sections. The geometry and the control variables are the same as those from the previous sections.

As expected, since the rotor does not achieve a fully periodic state within 2 revolutions, the rotors are now untrimmed for the subsequent revolutions, however the trim constraint is violated by the same amount by the three rotors, as shown in

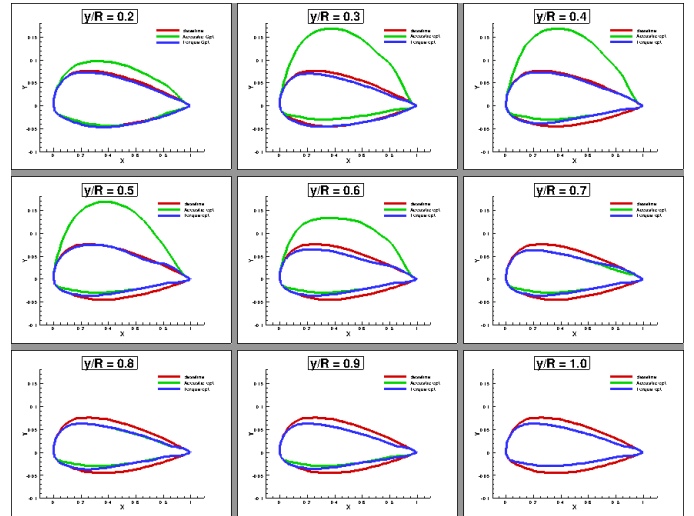
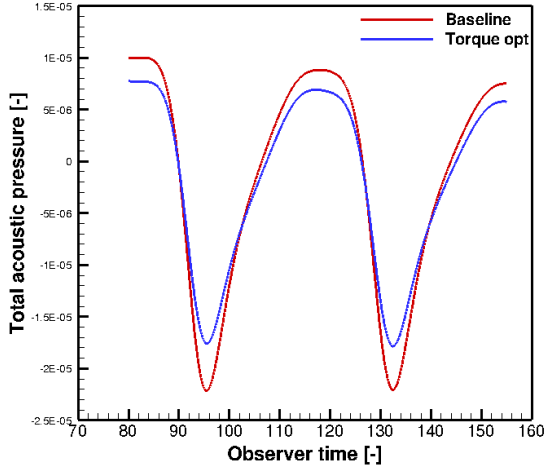


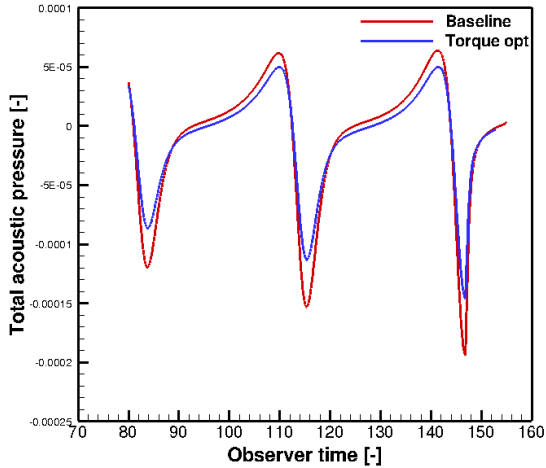
Fig. 20: Acoustically constrained torque optimized blade shapes

Figure 22, allowing for a meaningful comparison of the acoustic signature and of the required torque. The observer acoustic pressure time histories, shown in Figure 23, confirm the results from the previous sections: the aeroacoustically optimized rotor yields the biggest noise signature reduction when compared to the baseline rotor with a noise reduction of 2.7 dB OSPL at the observer, however the required torque is significantly increased, as shown in Figure 24. The acoustically constrained torque optimized rotor yields 2.9% reduction in required torque with a 1.9 dB OSPL reduction in noise signature.

These results show that even if the optimizations targeted only the second rotor revolution, they still have been able to improve rotor performance over multiple rotor revolutions. The resulting optimal rotors can be used as initial guesses for more expensive optimizations that target multiple rotor revolutions.



(a) Baseline and optimized total acoustic time history at $\psi = 135$ degrees



(b) Baseline and optimized total acoustic time history at $\psi = 315$ degrees

Fig. 21: Directivity study for the baseline and optimized geometry

CONCLUSIONS AND FUTURE WORK

Building upon the previously developed aeroelastic adjoint capability presented in (Refs. 20–22) and the aeroacoustic adjoint method presented in (Ref. 23) we developed a multidisciplinary adjoint capability that encompasses aerodynamics, aeroelasticity and aeroacoustics. The new multidisciplinary adjoint formulation has been successfully applied to the problem of noise minimization of the flexible Hart-II rotor in trimmed forward flight. The acoustically constrained torque minimization of the flexible HART-II rotor resulted in a rotor 2 dB quieter than the baseline with a 2.5% reduction in required torque highlighting the potential of high-fidelity multidisciplinary design optimization for rotorcraft design problems.

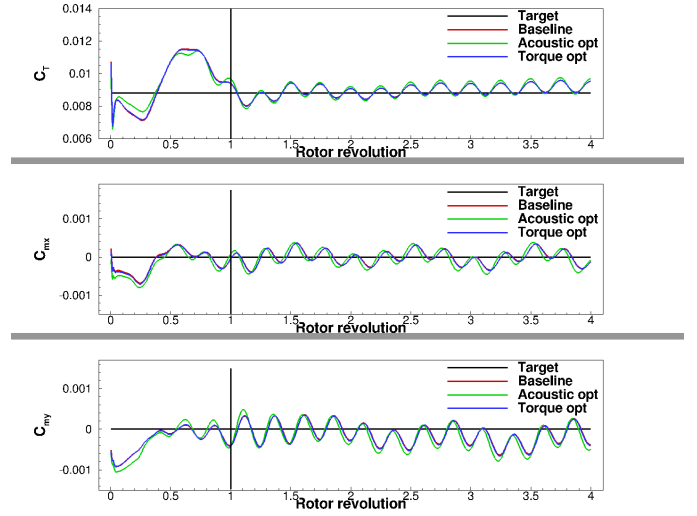


Fig. 22: Thrust and moments time histories for the baseline rotor, the aeroacoustic optimized rotor and the acoustically constrained torque optimized rotor over 4 rotor revolutions

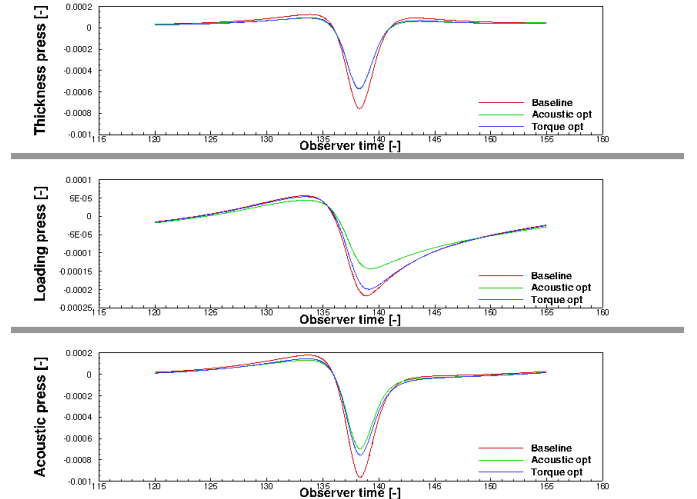


Fig. 23: Thickness, loading and total acoustic pressures at the observer for the baseline and the two optimized rotors for the multiple revolutions case.

Evaluation of the newly designed rotors over multiple rotor revolutions shows that, although the rotors are untrimmed, the trim constraint violation is the same for all the rotors and the performance and acoustic improvements gained with the current optimizations are kept even over longer simulation times, suggesting that the new rotors can be used as initial guesses for optimizations that target multiple rotor revolutions. In future work we will consider optimizing the rotor over multiple rotor revolutions and the inclusion of additional design variables to account for planform shape changes. Different acoustic problems, e.g. a wind-tunnel formulation, will also be considered.

ACKNOWLEDGEMENTS

This work was partly funded by the Alfred Gessow Rotorcraft Center of Excellence through a subcontract with the Univer-

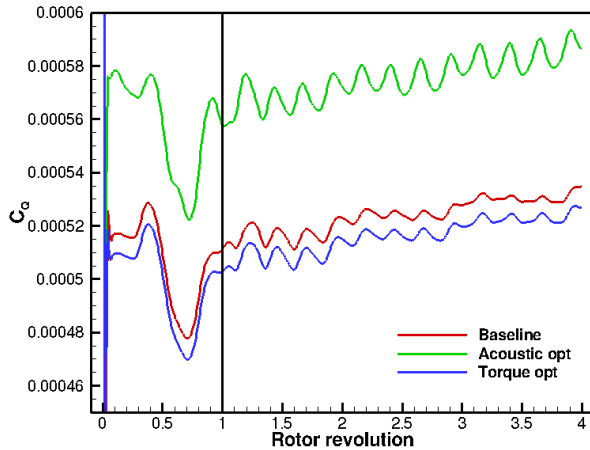


Fig. 24: Torque time histories for for the baseline rotor, the aeroacoustic optimized rotor and the acoustically constrained torque optimized rotor over 4 rotor revolutions

sity of Maryland. Computer resources were provided by the University of Wyoming Advanced Research Computing Center and by the NCAR-Wyoming Supercomputer Center. Special thanks Dr. Brentner for making PSU-WOPWOP available to us for validation purposes.

REFERENCES

- ¹Edwards, B. and Cox, C., “Revolutionary concepts for Helicopter Noise Reduction - S.I.L.E.N.T Program,” Technical Report CR-2002-211650, NASA, May 2002.
- ²Yu, Y. H., “Rotor blade vortex interaction noise,” *Progress in Aerospace Sciences*, Vol. 36, 2000, pp. 97–115.
- ³Sim, B. W., JanakiRam, R. D., Barbely, N. L., and Solis, E., “Reduced In-Plane, Low Frequency Noise of an Active Flap Rotor,” American Helicopter Society 65th Annual Forum, May 2009.
- ⁴Johnson, W., *Rotorcraft Aeromechanics*, Cambridge University Press, 2013.
- ⁵Dunn, M. H. and Farassat, F., “High-Speed Propeller Noise Prediction - A Multidisciplinary approach,” *AIAA Journal*, Vol. 30-7, 1992, pp. 1716–1723.
- ⁶Rumpfkeil, M. and Zingg, D., “A General Framework for the Optimal Control of Unsteady Flows with Applications,” 45th AIAA Aerospace Sciences Meeting and Exhibit, Reno, NV, January, AIAA Paper 2007–1128, 2007.
- ⁷Fabiano, E., Mavriplis, D. J., and Sitaraman, J., “Adjoint - based Aeroacoustic Design Optimization for Blade Vortex Interaction Noise,” 53rd AIAA Aerospace Sciences Meeting, AIAA Paper 2015–1801, January 4–8 2015.
- ⁸Rallabhandi, S. K., Nielsen, E. J., and Diskin, B., “Sonic Boom Mitigation Through Aircraft Design and Adjoint Methodology,” 30th AIAA Applied Aerodynamics Conference, AIAA Paper 2012–3220, 2012.
- ⁹Marinus, B. G., Roger, M., den Braembussche, V., and Bosschaerts, W., “Multidisciplinary optimization of propeller blades: Focus on acoustic results,” 47th AIAA/ASME/SAE/ASEE Joint Propulsion Conference and Exhibit, AIAA Paper 2011–2801, 2011.
- ¹⁰Jameson, A., “Aerodynamic Shape Optimization using the Adjoint Method,” VKI Lecture Series on Aerodynamic Drag Prediction and Reduction, von Karman Institute of Fluid Dynamics, Rhode St Genese, Belgium, 2003.
- ¹¹Lyu, Z., Kenway, K. W., and Martins, J. R. R. A., “Aerodynamic Shape Optimization Investigation of the Common Research Model Wing Benchmark,” *AIAA Journal*, Vol. 53-4, 2015, pp. 968–985.
- ¹²Bisson, F. and Nadarajah, S., “Adjoint-Based Aerodynamic Optimization of Benchmark Problems,” 53rd AIAA Aerospace Sciences Meeting, Kissimmee, FL, AIAA Paper 2015-1948, January 2015.
- ¹³Lee, C., Telidetzki, K., Buckley, H., Gagnon, H., and Zingg, D. W., “Aerodynamic Shape Optimization of Benchmark Problems Using Jetstream,” 53rd AIAA Aerospace Sciences Meeting, Kissimmee, FL, AIAA Paper 2015-0262, January 2015.
- ¹⁴Nadarajah, S. and Jameson, A., “Optimal Control of Unsteady Flows using A Time Accurate Method,” Proceedings of the 9th AIAA/ISSMO Symposium on Multidisciplinary Analysis and Optimization Conference, Atlanta GA, AIAA Paper 2002–5436, 2002.
- ¹⁵Mavriplis, D. J., “Solution of the Unsteady Discrete Adjoint for Three-Dimensional Problems on Dynamically Deforming Unstructured Meshes,” Proceedings of the 46th AIAA Aerospace Sciences Meeting, Reno, NV, AIAA Paper 2008–0727, 2008.
- ¹⁶Nielsen, E. and Diskin, B., “Discrete Adjoint-Based Design for Unsteady Turbulent Flows on Dynamic Overset Unstructured Grids,” 50th AIAA Aerospace Sciences Meeting and Exhibit, Nashville, TN, AIAA Paper 2012–0554, January 9-12 2012.
- ¹⁷Nielsen, E., Diskin, B., and Yamaleev, N. K., “Discrete Adjoint-Based Design Optimization of Unsteady Turbulent Flows on Dynamic Unstructured Grids,” *AIAA Journal*, Vol. 48, (6), June 2010, pp. 1195–1206.
- ¹⁸Jones, W. T., Nielsen, E., Lee-Rausch, E. M., and Acree, C. W., “Multi-Point Adjoint-Based Design of Tilt-Rotors in a Noninertial Reference Frame,” AIAA Paper 2014 – 0290, January 2014.
- ¹⁹Mani, K. and Mavriplis, D. J., “Geometry Optimization in Three-Dimensional Unsteady Flow Problems using the Discrete Adjoint,” 51st AIAA Aerospace Sciences Meeting, Grapevine, TX, AIAA Paper 2013-0662, January 2013.

- ²⁰Mishra, A., Mani, K., Mavriplis, D. J., and Sitaraman, J., “Helicopter Rotor Design using Adjoint-based Optimization in a Coupled CFD-CSD Framework,” 69th American Helicopter Society Annual Forum, Phoenix, AZ, May 21–23 2013.
- ²¹Mishra, A., Mani, K., Mavriplis, D. J., and Sitaraman, J., “Time-dependent Adjoint-based Optimization for Coupled Aeroelastic Problems,” 21st AIAA CFD Conference, San Diego, CA, AIAA Paper 2013–2906, June 24–27 2013.
- ²²Mishra, A., Mani, K., Mavriplis, D. J., and Sitaraman, J., “Time-dependent Adjoint-based Aerodynamic Shape Optimization Applied to Helicopter Rotors,” 70th American Helicopter Society Annual Forum, Montreal, QC, CA, May 20–22 2014.
- ²³Fabiano, E., Mishra, A., Mavriplis, D., and Mani, K., “Time-dependent Aero-acoustic Adjoint-based Shape Optimization of Helicopter Rotors in Forward Flight,” 57th AIAA/ASCE/AHS/ASC Structures, Structural Dynamics and Material Conference, AIAA Paper 2016–1910, 2016.
- ²⁴Mavriplis, D. J., “Solution of the Unsteady Discrete Adjoint for Three-Dimensional Problems on Dynamically Deforming Unstructured Meshes,” Proceedings of the 46th Aerospace Sciences Meeting and Exhibit, Reno NV, AIAA Paper 2008–0727, 2008.
- ²⁵Mavriplis, D. J., “Discrete Adjoint-Based Approach for Optimization Problems on Three-Dimensional Unstructured Meshes,” *AIAA Journal*, Vol. 45-4, April 2007, pp. 741–750.
- ²⁶Spalart, P. R. and Allmaras, S. R., “A One-equation Turbulence Model for Aerodynamic Flows,” *La Recherche Aéronautique*, Vol. 1, 1994, pp. 5–21.
- ²⁷Mavriplis, D. J. and Mani, K., “Unstructured Mesh Solution Technique Using the NSU3D Solver,” Proceedings of the 52nd AIAA Aerospace Sciences Conference, National Harbor, MD, AIAA Paper 2014–0081, 2014.
- ²⁸Mavriplis, D. J., Yang, Z., and Long, M., “Results using NSU3D for the first Aeroelastic Prediction Workshop,” Proceedings of the 51st Aerospace Sciences Meeting and Exhibit, Grapevine TX, AIAA Paper 2013–0786, 2013.
- ²⁹Schuster, D. M., Chwalowski, P., Heeg, J., and Wieseman, C. D., “Summary of Data and Findings from the First Aeroelastic Prediction Workshop,” Seventh International Conference on Computational Fluid Dynamics (ICCFD7), July 9-13 2012.
- ³⁰Yu, Y. H., Tung, C., van der Wall, B., Pausder, H.-J., Burley, C., Brooks, T., Beaumier, P., Delrieux, Y., Mercker, E., and Pengel, K., “The HART-II Test: Rotor Wakes and Aeroacoustics with Higher-Harmonic Pitch Control (HHC) Inputs - The Joint German/French/Dutch/US Project-,” 58th American Helicopter Society Annual Forum, Montreal, Canada, June 11–13 2002.
- ³¹Chopra, I. and Bir, G., “University of Maryland Advanced Rotor Code: UMARC,” American Helicopter Society Aeromechanics Specialists Conference, January 1994.
- ³²Heckmann, A. Otter, M., Dietz, S., and Lopez, J. D., “The DLR FlexibleBodies Library to Model Large Motions of Beams and of Flexible Bodies Exported from Finite Element Programs,” *Modelica*, September 4–5 2006.
- ³³Kumar, A. A., Vishwamurthy, S. R., and Ganguli, R., “Correlation of helicopter rotor aeroelastic response with HART-II wind tunnel test data,” *Aircraft Engineering and Aerospace Technology: An International Journal*, Vol. 82, (4), 2010, pp. 237–248.
- ³⁴Yang, Z. and Mavriplis, D. J., “A Mesh Deformation Strategy Optimized by the Adjoint Method on Unstructured Meshes,” *AIAA Journal*, Vol. 45, (12), 2007, pp. 2885–2896.
- ³⁵Brentner, K. S. and Farassat, F., “Modeling aerodynamically generated sound of helicopter rotors,” *Progress in aerospace sciences*, Vol. 39, 2003, pp. 83–120.
- ³⁶Crighton, D. G., Dowling, A. P., and Ffowcs Williams, J. E., *Modern Methods in Analytical Acoustics*, Springer-Verlag, 1992.
- ³⁷Brentner, K. S. and Farassat, F., “An Analytical Comparison of The Acoustic Analogy And Kirchoff Formulation For Moving Surfaces,” *AIAA Journal*, Vol. 36-8, 1998, pp. 1379–1386.
- ³⁸Farassat, F. and Succi, G. P., “The prediction of helicopter discrete frequency noise,” *Vertica*, Vol. 7-4, 1983, pp. 309–320.
- ³⁹di Francescantonio, P., “A New Boundary Integral Formulation for the Prediction of Sound Radiation,” *Vertica*, Vol. 7-4, 1983, pp. 309–320.
- ⁴⁰Bres, G. A., Brentner, K. S., Perez, G., and Jones, H. E., “Maneuvering rotorcraft noise prediction,” *Journal of sound and vibration*, Vol. 275, 2004, pp. 719–738.
- ⁴¹Martins, J. R. R. A. S. P. and Alonso, J. J., “The Complex-Step Derivative Approximation,” *ACM Transactions on Mathematical Software*, Vol. 29-3, 2003, pp. 245–262.
- ⁴²Mishra, A., Mavriplis, D. J., and Sitaraman, J., “Time-dependent Aero-elastic Adjoint-based Aerodynamic Shape Optimization of Helicopter Rotors in Forward Flight,” *AIAA journal*, Accepted for publication.
- ⁴³Gill, P. E., Murray, W., and Saunders, M. A., “SNOPT: An SQP Algorithm for Large-Scale Constrained Optimization,” *SIAM review*, Vol. 47-1, 2005, pp. 99–131.